Spatially resolved Fourier transform impedance spectroscopy: A technique to rapidly characterize interfaces, applied to a QD/SiC heterojunction

Cite as: Appl. Phys. Lett. **118**, 223102 (2021); https://doi.org/10.1063/5.0046439 Submitted: 03 February 2021 . Accepted: 14 May 2021 . Published Online: 01 June 2021

hathew L. Kelley, Grigory Simin, Kamal Hussain, Asif Khan, Andrew B. Greytak, M. V. S. Chandrashekhar, et al.







ARTICLES YOU MAY BE INTERESTED IN

Perspective on the future of silicon photonics and electronics
Applied Physics Letters 118, 220501 (2021); https://doi.org/10.1063/5.0050117

Enhanced far ultraviolet spectral response and gain in SiC avalanche photodiodes Applied Physics Letters 118, 221102 (2021); https://doi.org/10.1063/5.0050046

2DEGs formed in AIN/GaN HEMT structures with AIN grown at low temperature Applied Physics Letters 118, 222103 (2021); https://doi.org/10.1063/5.0050584





Spatially resolved Fourier transform impedance spectroscopy: A technique to rapidly characterize interfaces, applied to a QD/SiC heterojunction

Cite as: Appl. Phys. Lett. **118**, 223102 (2021); doi: 10.1063/5.0046439 Submitted: 3 February 2021 · Accepted: 14 May 2021 · Published Online: 1 June 2021







Mathew L. Kelley, b Grigory Simin, Kamal Hussain, b Asif Khan, b Andrew B. Greytak, h and M. V. S. Chandrashekhar h ar fip

AFFILIATIONS

- Department of Chemistry and Biochemistry, University of South Carolina, Columbia, South Carolina 29208, USA
- ²Department of Electrical and Computer Engineering, University of South Carolina, Columbia, South Carolina 29208, USA
- ³USC Nanocenter, University of South Carolina, Columbia, South Carolina 29208, USA

ABSTRACT

We demonstrate a technique to quickly build and spatially map the frequency response of optoelectronic devices. The transfer function of a linear system is the Fourier transform of its impulse response. Such an impulse response is obtained from transient photocurrent measurements of devices such as photodetectors and solar cells. We introduce and apply Fourier transform impedance spectroscopy (FTIS) to a PbS colloidal quantum dot SiC heterojunction photodiode and validate the results using intensity-modulated photocurrent spectroscopy. Cutoff frequencies in the devices were as high as \sim 10 kHz, showing their utility in advanced thin film and flexible electronics. The practical frequencies for FTIS lie in the mHz-kHz range, ideal for composite materials such as quantum dot films that are dominated by interfacial trap states. These can lead to characteristic lengths for charge collection \sim 20–500 μ m dominated by transmission line effects, rather than intrinsic diffusion and drift length scales, enabling extraction of interfacial capacitances and series/parallel resistances.

Published under an exclusive license by AIP Publishing. https://doi.org/10.1063/5.0046439

Rapid characterization of junction parameters and film properties is crucial for optimizing optoelectronic devices. This is particularly relevant to novel materials and thin film devices, such as colloidal quantum dot (QD) photovoltaics and mixed-dimensional heterostructures, where interfaces and structural imperfections can dominate. 1-3 In this regard, frequency domain and time domain characterization methods are commonly employed to obtain information on defects, trapping, 5 and recombination, making them valuable tools for such purposes. Most commonly, impedance spectroscopy (IS) is an appealing nondestructive ensemble technique performed in the frequency domain. An IS experiment is undertaken by applying a sinusoidal input voltage to the sample and measuring the output sinusoidal current response as a function of frequency. By modeling the device with equivalent circuit elements, details on resistive and capacitive quantities, such as the series resistance or charge transfer resistances of solar photovoltaics,^{7–9} can be obtained. From quantities such as these, IS is used to optimize devices by studying these characteristics' sensitivity to device parameters, such as contact metals or chemical modifications to active layers. Intensity-modulated photocurrent spectroscopy (IMPS) is a closely

related technique to IS that employs light-induced perturbations at varying frequency to extract information on resistive and capacitive elements and charge transport processes within an optoelectronic device.

Despite the merits of these frequency domain methods, characterizing composite materials holds challenges. For example, IS and IMPS require small signals to be linearized with circuit elements, presenting a trade-off in terms of signal level with accuracy. In addition, for low dimensional materials, such as quantum dots (QDs), capacitive elements manifesting from trap states¹⁰ and interfaces impart slow device bandwidths¹¹ and necessitate low frequency perturbations, compounding the experimental run time. These challenges are also encountered in scanning measurement techniques such as scanning photoinduced impedance spectroscopy¹² and scanning IMPS¹³ methods, where the appeal of establishing spatial correlation with localized impedances are hindered by the time investment of multiple scans in the low frequency regime.

Beyond the frequency domain methods of IS and IMPS, pure time domain techniques, such as deep level transient spectroscopy (DLTS)^{14,15} or current-deep level transient spectroscopy (i-DLTS),

^{a)}Authors to whom correspondence should be addressed: greytak@sc.edu and chandra@cec.sc.edu

provide information on trap states, but they require temperature dependent measurements, which are time-consuming and challenging. Due to the trade-offs and time required for these techniques, exploring alternative methods to characterize interfaces in a rapid manner is useful.

Here, we introduce a method in the time domain to quickly build the frequency response of a device by computing the Fourier transform of a transient photocurrent.

In any linear, time invariant system¹⁶ (or any system that can be linearized by operating at small signals^{16,17}), the output response, $x_{out}(t)$ to an input signal, $x_{in}(t)$ is characterized in the time domain by the impulse response h(t), which is the output when the input is a Dirac delta function, $\delta(t)$. The output $x_{out}(t)$ is given by the convolution of $x_{in}(t)$ with h(t), ¹⁶

$$x_{out}(t) = \int_{-\infty}^{+\infty} x_{in}(t-\tau)h(\tau)d\tau. \tag{1}$$

For a sinusoidal input, $x_{in}(t) = \exp(j\omega t)$, the output can be written as

$$x_{out}(t) = \exp(j\omega t) \int_{-\infty}^{+\infty} \exp(-j\omega \tau) h(\tau) d\tau,$$
 (2a)

$$x_{out}(t) = H(\omega)x_{in}(t),$$
 (2b)

so that the system is represented in the frequency domain by the transfer function $H(\omega)$, which is shown to be the Fourier transform of the broadband impulse response h(t), i.e.,

$$H(\omega) = \mathcal{F}(h(t)) = \int_{-\infty}^{+\infty} \exp(-j\omega\tau)h(\tau)d\tau. \tag{3}$$

In practice, it is difficult to generate an impulse input. Using the linearity of the devices under study, we instead use the step response, s(t), which is the output for a unit step input, u(t), provided by turning an electrical or an optical source on (or off). Just as $\delta(t)$ is the derivative of u(t), the impulse response, h(t), is computed by

$$h(t) = \frac{ds(t)}{dt}. (4)$$

Once h(t) is obtained, the frequency response $H(\omega)$ is directly known via a numerical Fourier transform (Fig. 1). The frequency limits of this measurement are determined by how quickly x_{out} can be measured. If the transient is sampled every $T_{\rm s}\sim 1\,{\rm ms}$ (i.e., sampling frequency of 1 kHz), a high frequency Nyquist 16 limit $f_{\rm max} = 1/2T_{\rm s} \sim 500\,{\rm Hz}$ is obtained. The lower frequency limit, f_{\min} , is determined by the overall transient acquisition time. For an acquisition time T_a of 10 s at $T_s = 1$ ms, the total number of samples is $T_a/T_s = 10^4$, giving $f_{min} = f_{max}/(T_a/2T_s) = 0.1$ Hz, where the extra factor of 2 arises from negative frequencies for real signals. 16 A comparable measurement in the frequency domain would require at least 10 cycles for each frequency point, leading to >100 s for just the 0.1 Hz point alone, underscoring the greater speed of Fourier transform impedance spectroscopy (FTIS). This is because the pulse that generates s(t) is broadband, i.e., contains a large range of frequencies by Fourier's therorem.16

These ranges are ideal for characterizing polymer and composite materials with typical response times in the ms-min range. The low frequency range is particularly tantalizing given the challenges in

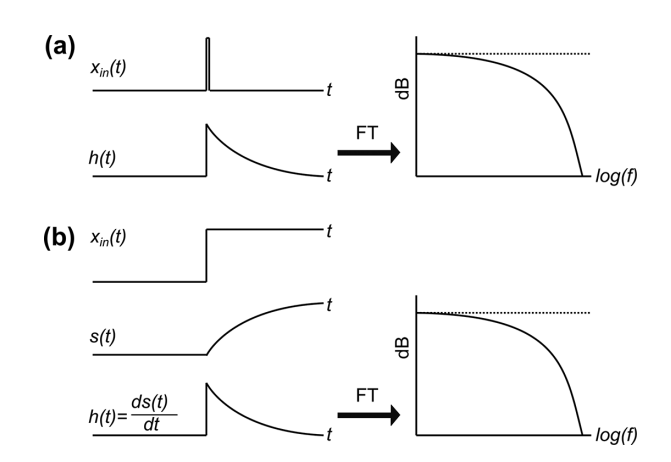


FIG. 1. Graphic illustrating the application of Fourier theorem and the transformation to achieve the frequency response from (a) an impulse response and (b) a step-up response.

generating stable waveform inputs at low frequencies and small amplitudes 16 using mechanical chopping, or digital modulation for photoexcitation. In our measurements, typical photocurrent signal levels for transient measurements lie in the nA- μ A range, whereas higher frequency measurements provide pA level currents, 3 requiring sensitive lock-in techniques.

The higher overall signal levels in the FTIS technique presents another advantage. Fourier transforms have been used in infrared, 20 Raman,²¹ and electrochemical impedance²² spectroscopies owing to the same data acquisition speed and other advantages outlined here. Fourier transform methods have also been applied to voltage and optical step function excitation of polymer solar cells, but is here combined with localized excitation to isolate a single planar interface by probing lateral signal propagation. We targeted QD/SiC photodiodes as a representative test platform to apply this transient Fourier technique. We have recently demonstrated that p-type PbS QDs can form an IR-sensitive photodiode junction with an *n*-type single-crystal SiC substrate. As shown in Fig. 2(a), our device includes epitaxial graphene (EG) electrodes, grown on the substrate prior to QD deposition as an effective Ohmic contact to the QD film. The EG forms a Schottky contact to the SiC, such that current at reverse bias (and small forward bias) is dominated by the QD/SiC junction. PbS QD/SiC junctions with epitaxial graphene (EG) electrodes are formed upon deposition of the QD layer. Previously, we showed that these devices exhibit photoresponses determined by the PbS QD's effective bandgap, while the effective transport length is the transfer length (L_T) of the QD/SiC heterojunction, determined by transmission line effects rather than diffusion/drift, from which we determined the shunt and sheet resistances.²³ Because L_T extends to many micrometers at low frequency, we are able to selectively excite the QD/SiC interface in spatially resolved FTIS measurements. We demonstrate that, in this manner, FTIS can be used to additionally obtain the junction capacitance. We validate FTIS independently with IMPS, yielding cutoff frequencies in the $\sim 10 \, \text{kHz}$ regime. The bandwidth of EG/SiC heterostructures² and QD detectors²⁶ is such that spatially resolved FTIS offers a substantial speed advantage in accomplishing the measurement.

PbS QDs with an effective bandgap of \sim 927 nm (\sim 1.3 eV, diameter \sim 3 nm) were synthesized as reported in Ref. 27. The QDs

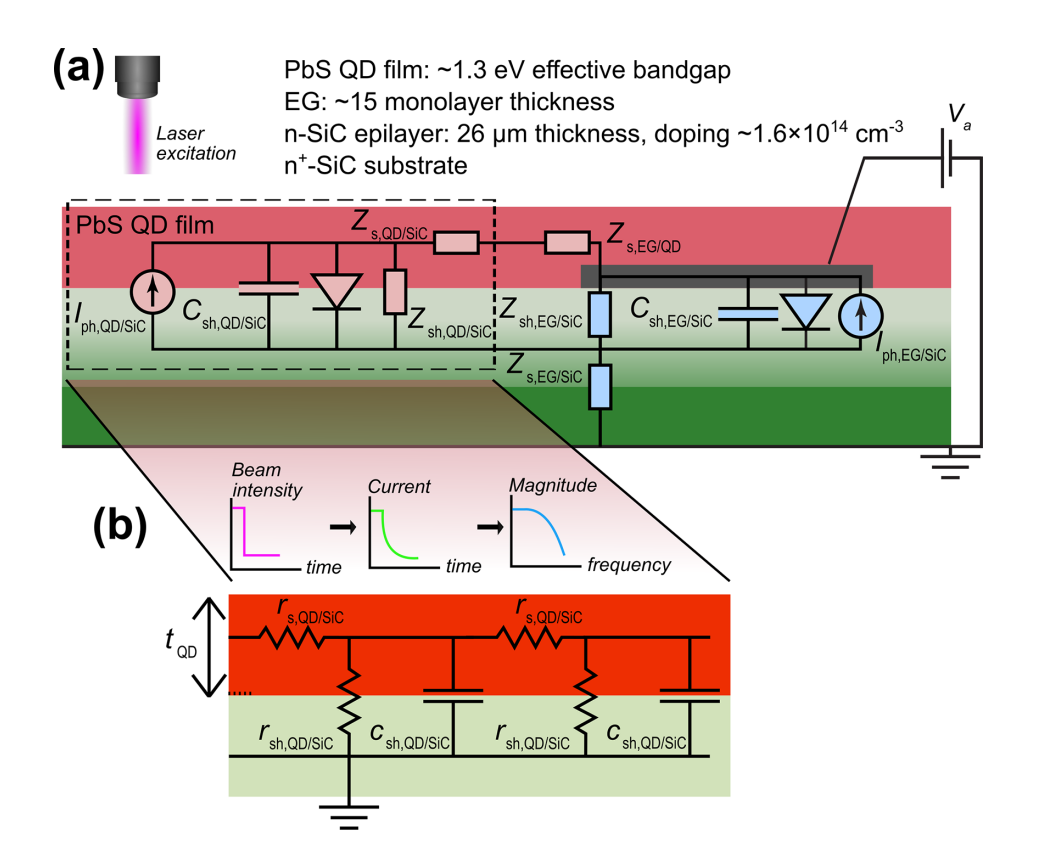


FIG. 2. (a) Equivalent circuit diagram of the QD/epitaxial graphene (EG)/SiC hybrid device with the QD/SiC interface outlined by the dashed box. Diode elements and associated photocurrents are also indicated. (b) Transmission line model for lateral photocurrent propagation in the QD film, showing series impedances of the QD film and shunt impedances and shunt capacitances for the QD/SiC interface, per unit width, that determine the frequency response at different distances from the EG contact as measured by spatially resolved FTIS.

were then purified using gel permeation chromatography, 23,28,29 arriving at an oleate surface ligand population of ~110/QD as determined by nuclear magnetic resonance (NMR) (Fig. S1). The diameter was estimated from a sizing curve based on the lowest-energy excitonic absorption peak.²⁷ Using a n^+ 4H-SiC substrate with an n-type epilayer, EG/n-SiC Schottky diodes were grown and then patterned by photolithography. The state of the devices was characterized prior to QD deposition (Fig. S2) by spot I-V measurements and scanning photocurrent microscopy (SPCM) at 444 nm, with results consistent with our previous report.²³ A layer-by-layer spin coating process (three cycles total, in a nitrogen-filled glovebox) was used to deposit a QD film and accomplish ligand exchange with 1,2-ethanedithiol (EDT) to form the QD/EG/SiC hybrid device structure. Atomic force microscopy was taken in the same manner as before. Spot I-Vs, FTIS, and IMPS were acquired in the same manner as for the bare EG/SiC control.²³ FTIS with spot illumination was undertaken as follows. Devices were held under a constant bias with the 444 nm diode laser modulated by an external control signal (Toptica, <500 ns rise as configured) defocused to form a \sim 25 μ m spot size through an objective lens (20×, 0.42 NA). Photocurrent was routed through a current preamplifier to a digital oscilloscope to record transients. For comparison, IMPS spectra with spot illumination were obtained by routing photocurrent through a current preamplifier to a network analyzer.

For our measurement setup, the noise floor is given by the measured²⁵ noise spectral density of 10^{-24} A²/Hz, and the maximum frequency of 10 kHz for these devices, giving a rms noise current of \sim 100 pA. Our measured responsivity for this device was \sim 1.6 \times 10⁻⁴ A/W at 444 nm, which gives an optical noise equivalent power

(NEP) of $0.6\,\mu\mathrm{W}$. The power in the beam used for both measurements was $0.2~\mathrm{mW}$, which is $300\times$ the NEP, i.e., both FTIS and IMPS measurements are not noise limited. We used 50% duty cycle for both measurements. FTIS, IMPS, and spot I-Vs were conducted under the same illumination conditions and locations under ambient conditions. The impulse response was stable over multiple cycles: averaging of up to 64 individual responses (\sim 3 s total at 20 Hz) was found to improve signal to noise for FTIS, but did not qualitatively change the frequency response.

Figure 3 shows static I-V curves of the QD/EG/SiC photodiodes in the dark and under illumination at various distances from the edge of the \sim 250 μ m diameter EG electrode. The DC photocurrent decreases away from the EG electrode edge. A traditional explanation would attribute this decay to charge collection near the electrode. However, in our previous paper, we demonstrated that this was due to transmission line effects instead. The characteristic length scale for a transmission line is L_T , which describes the transfer of electrical current across an electrical interface. For a lumped element resistance-conductance-capacitance (RGC) transmission line model [Fig. 2(b)], 31,32

$$1/L_{T} = \sqrt{r_{s} \left(\frac{1}{r_{sh}} + j\omega c_{sh}\right)} = \sqrt{\frac{\rho_{QD}}{t_{QD}} \left(\frac{1}{R_{sh,QD/SiC}} + j\omega C_{sh,QD/SiC}\right)},$$
(5)

where ρ_{QD} is the 3D resistivity of the QD film, and t_{QD} is the thickness of the QD film. Shunting conductances denoted by G in the RGC model are represented here by resistive elements per G=1/R, with $R_{sh,OD/SiC}$ specifying the specific shunt resistance at the QD/SiC

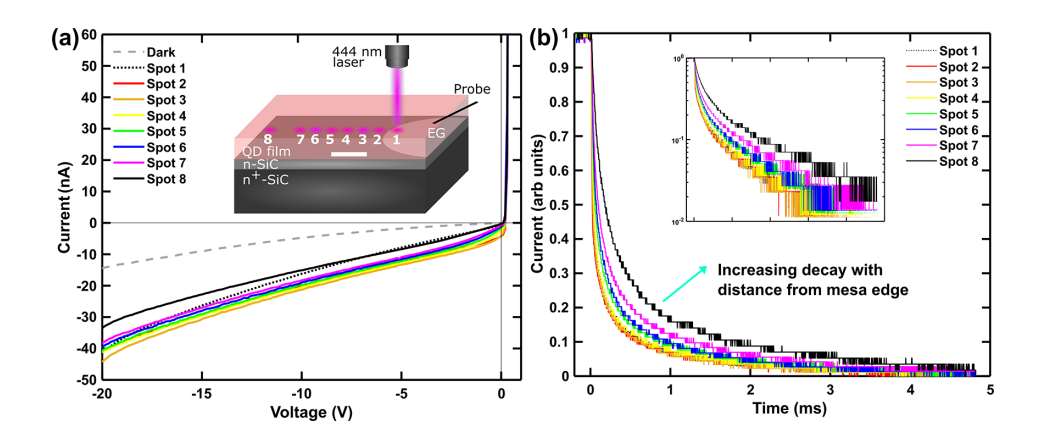


FIG. 3. (a) Static I–V curves with spot illumination at 444 nm (\sim 186 μ W). Inset shows the device schematic and general spot illumination regions for I–Vs, FTIS, and IMPS measurements. (b) Normalized 20 V reverse bias photocurrent transients under the same spot illumination intensity and locations. Inset shows transients on a semilogarithmic scale.

interface (in Ω -cm²), and $C_{sh,QD/SiC}$ as the specific areal shunting capacitance (in F-cm⁻²). At low frequencies, shunting capacitances are open circuits, and only the resistances are needed to quantify L_T as in our prior work.²³ At high frequencies, the capacitances short out and dominate current flow through the QD/SiC junction, leading to shorter L_T . The cutoff angular frequency $\omega_c = (R_{sh,QD/SiC}C_{sh,QD/SiC})^{-1}$, at which the phase change is 22.5° for transmission lines, rather than the 45° for a proper single pole response.¹⁶

In the low frequency regime, using $t_{QD}\sim 140$ nm (Fig. S1), $L_T\sim 270~\mu m$ from SPCM (Fig. S3) as defining the active device area, and the total shunt resistance $R_{sh}\sim 270~\mathrm{M}\Omega$ from I-V measurements [Fig. 3(a)] of the QD/EG/SiC device, we obtain a $R_{sh,QD/SiC}\sim 1.2~\mathrm{M}\Omega\text{-cm}^2$, larger than the 260 k Ω -cm obtained in our previous work. The extracted ρ_{QD} of $\sim 22~\mathrm{k}\Omega$ -cm was comparable to our previous report with larger PbS QDs (4.5 nm diameter). ²³

The comparable ρ_{QD} , but $\sim 5 \times$ larger $R_{sh,QD/SiC}$ suggests the formation of a cleaner QD/SiC interface. The ligand exchange conditions could have facilitated this. A systematic study by Kirmani³³ indicated optimal conditions for solid-state exchanged PbS QD (3.2 nm size) films with EDT included ligand solution concentrations $\sim 0.01\%$ v/v. The ligand concentration here was lower ($\sim 0.4\%$ v/v) than our previous work (1% v/v) with larger QDs.²³ We speculate that implementing a more optimal ligand exchange process and better infilling ^{33,34} by smaller QDs on the rough (~ 10 nm rms) SiC³⁵ surface facilitated the formation of a superior QD/SiC junction.

Photocurrent transients at 20 V reverse bias for each location displayed in Fig. 3(b) show multi-exponential decays, as observed previously.²³ These decays increased distinctly in lifetime with distance from the EG edge. Although variations in photocurrent decays have been affiliated with localized defects in transient photocurrent mapping reports on organic photovoltaics, 36 we do not attribute the increase in decay times to such imperfections given the broadly homogeneous decay of the SPCM signal (Fig. S3) from the EG edge. We reason that the increase in photocurrent decay times with distance indicated an increasing series resistance in the QD film (Fig. 2), consistent with our past report. Contributions to the photoresponse from absorption in the underlying SiC substrate were negligible: in bare EG/ SiC devices (Fig. S4), a low but nonzero photocurrent transient with lifetime <0.1 ms off the edge of the EG mesa region was observed, contrasting with larger photocurrent and relatively longer lifetimes $(\sim 2 \text{ ms})$ observed in QD/EG/SiC hybrids.

The Fourier transform of photocurrent transients was used to obtain corresponding frequency responses of the QD/SiC devices. Figures 4(a) and S5 show the frequency dependence measured explicitly by IMPS (\sim 90 s for each measurement), and that extracted from FTIS (<3.5 s for each measurement) overlaid. The two methods have excellent agreement both in magnitude and phase, showing the simplicity, accuracy, and speed of FTIS over more complex traditional frequency domain techniques. The frequency response of the bare EG/SiC photodiode was consistent for both FTIS and IMPS (Fig. S6). Notably, the f_{3dB} bandwidth of both bare and QD/SiC photodiodes was \sim 10 kHz, comparable to other heterostructure optoelectronics employing low dimensional materials. 19,26

Spatial and frequency dependencies obtained by the two methods are combined in Figs. 4(b) and 4(c). The L_T for each frequency is the distance that the signal decreases to 1/e, or a power loss of 1/e² (i.e., $20 \cdot \log_{10}(e) = \sim 8.7$ dB) from the EG mesa edge. 31,32 The trend is shown in both IMPS and FTIS where low and high frequencies correspond to resistive and capacitive dominated regimes, respectively.

Bias-dependent mapping of the QD/EG/SiC photodiode frequency response was employed to characterize capacitive elements. Figure 5 shows L_T extracted from Figs. 4 and S7 plotted as a function of frequency for three different QD/SiC photodiode biases, with overlaid lines indicating fits from Eq. (5) to obtain the QD/SiC specific junction capacitances. We infer a decrease in $C_{sh,QD/SiC}$ with increasing reverse bias. We note that slower device transients with increasing reverse bias (Fig. S8) were observed.

Although such behavior is atypical of photodiodes, we attribute the observation to an increase in device area via L_T (Figs. 5 and S7). Given that $C_{sh,QD/SiC}$ decreases with increased reverse bias, it suggests that the key capacitance is the geometric depletion capacitance arising primarily from depletion in the n-SiC epitaxial layer. We do not see excess capacitance from trapping effects in the PbS CQD film, indicating that ligand-exchange 35,37 and packing density 38 have been well optimized. For the SiC geometrical capacitance (see supplementary material), accounting for a bare surface barrier of \sim 1 eV, comparable to the EG/SiC barrier, we estimate

$$C_{sh,QD/SiC} = \frac{\epsilon_{SiC} \cdot \epsilon_0}{\sqrt{\frac{2 \cdot \epsilon_{SiC} \cdot \epsilon_0}{q \cdot N_d} (1 + V_R)}},$$
(6)

which produces a value slightly (<50%) larger than experimental capacitance. The discrepancies may be due to (i) uncertainty in the

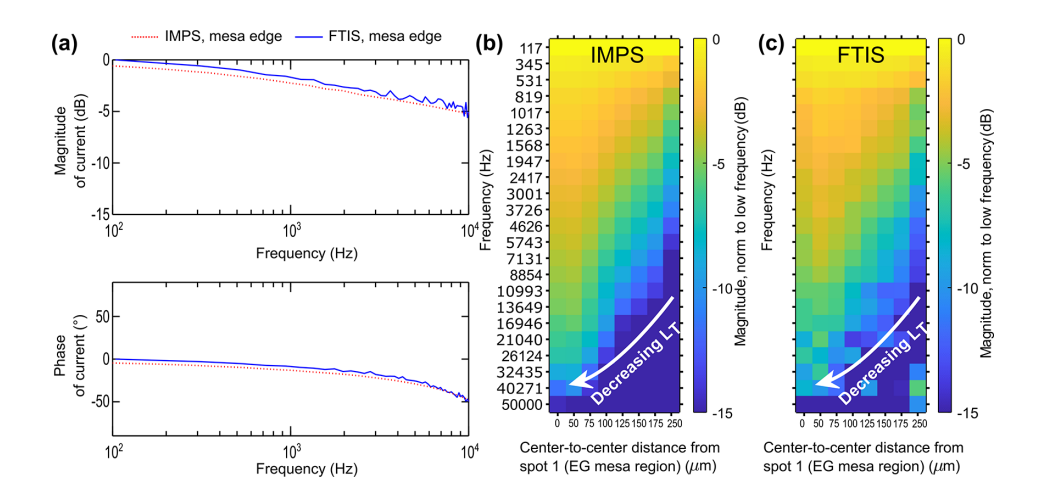


FIG. 4. Spatially resolved photocurrent by IMPS and FTIS at 20 V reverse bias with 444 nm excitation ($\sim\!186~\mu\mathrm{W}$). (a, top) shows the IMPS spot 2 spectra overlaid with the FTIS spectrum, with (a, bottom) displaying the corresponding phase spectra. (b) IMPS heat map showing position dependent photocurrent magnitude. (c) FTIS heat map. Magnitude spectra in [(a)–(c)] are normalized at low frequency for clarity.

SiC epitaxial layer doping extracted by capacitance–voltage at 100 kHz and/or (ii) the use of a one-dimensional approximation for the QD/SiC transmission line, which may become inaccurate at distances much greater than the device radius. Despite these uncertainties, the TLM model enabled the conclusive identification of geometrical capacitance as the limiting factor in the bandwidth of the CQD/EG/SiC photodiode. This is consistent with the findings here and our previous results, where SPCM at frequencies (~77–113 Hz) well below the cutoff ~10 kHz (Fig. 4) enabled us to safely treat the capacitances in the TLM as open circuits.

Key device features of the QD/EG/SiC hybrid studied here suggest the formation of a cleaner interface between the assembled QD film and underlying crystalline SiC layer than in our previous work. Response (fall) times for this device were less than \sim 2 ms, over an order of magnitude faster. However, lower responsivities were observed, suggesting lower trap assisted photoconductive gain at the heterojunction. ^{11,18,39,40} Finally, the fivefold larger $R_{sh,QD/SiC}$ than previously ²³ signifies a superior interface with reduced shunting conductance from traps. ^{39,41} Ultimately, these results highlight the importance of nanocrystal preparation (e.g., purification, ^{28,42} film

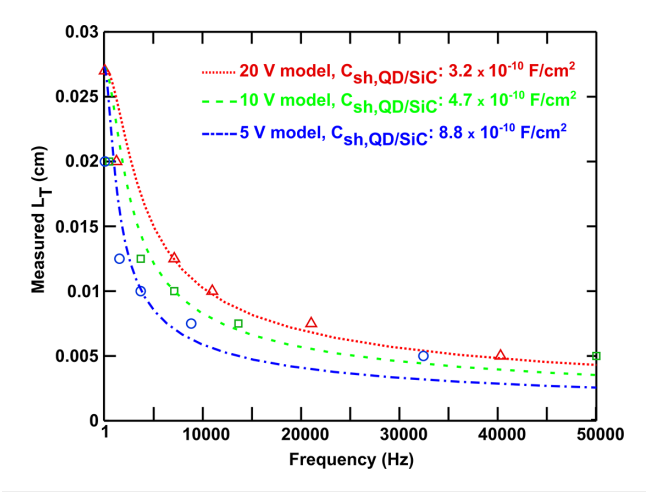


FIG. 5. Extracted transfer lengths (L_7) as a function of frequency for 20 V (\triangle) , 10 V (\Box) , and 5 V (\bigcirc) reverse bias conditions in a QD/EG/SiC hybrid device.

assembly³³) for combining solution processed materials with single crystal substrates^{39,40} to form clean heterojunctions. This is particularly attractive for wide bandgap (WBG) platforms, where dual functionality of the WBG material as an optical window and photoactive layer could be used in fast devices compatible with multiple wavelengths. Given notable advances in micropatterning^{43–45} and inkjet printing⁴⁶ for solution processed materials, monolithic photonics with pixel densities rapidly optimized by L_T through FTIS to balance sensitivity and bandwidth can be envisioned.

The proof of concept scanning FTIS technique presented here demonstrates that rapid spatial mapping of composite interfaces is possible. The method may be used for the extraction of characteristic lengths and interfacial properties, making it particularly advantageous as a rapid diagnostic method to merge speed, accuracy, and spatial registry vs conventional time domain techniques. In the present case, a smaller area Ohmic contact (EG) is used to extract current from a larger area QD/SiC rectifying junction. FTIS revealed the SiC geometric capacitance at the QD/SiC heterojunction to be the primary limiting factor of the device bandwidth. This was achieved without evaporation of a top contact, typically an architectural necessity in planar QD systems. Using small PbS QDs, we find that our QD/SiC interface is superior to the one in our previous report, possibly due to favorable post-synthetic purification^{28,42} and/or ligand exchange.³³ These findings underscore the ability to form clean junctions to single crystals with chemically prepared QDs. We anticipate that FTIS is applicable to other complex interfaces, including scalable solar cells and photodetectors with stripe contacts that diminish the need for transparent conductors, making it valuable beyond the platform studied here.

See the supplementary material for estimation of capacitance, UV-vis and ¹H NMR spectroscopy of PbS QDs prior to film deposition, AFM analysis of QD film, SPCM images of EG/SiC and QD/EG/SiC devices, and Figs. S1–S8.

This work was partially supported by the National Science Foundation (NSF), ECCS Award Nos. 1711322, 1810116, and 1831954. We also gratefully acknowledge the support through ARO Contract No. W911NF-18-1-0029 monitored by Dr. M. Gerhold, and by AFOSR through Dr. K. Goretta. M.L.K. was additionally

supported by an NSF IGERT graduate fellowship under Grant No. 1250052. Additional support from the University of South Carolina through the Aspire program is acknowledged. We gratefully acknowledge Anusha Balachandran for material growth, Surya Chava for device fabrication, and Modi Uddin Jewel for assistance with atomic force microscopy.

DATA AVAILABILITY

The data that support the findings of this study are available within the article and its supplementary material.

REFERENCES

- ¹R. Xiao, Y. Hou, Y. Fu, X. Peng, Q. Wang, E. Gonzalez, S. Jin, and D. Yu, "Photocurrent mapping in single-crystal methylammonium lead iodide perovskite nanostructures," Nano Lett. **16**, 7710 (2016).
- ²P. H. Rekemeyer, C.-H. M. Chuang, M. G. Bawendi, and S. Gradečak, "Minority carrier transport in lead sulfide quantum dot photovoltaics," Nano Lett. 17, 6221 (2017).
- ³B. G. Barker, V. S. N. Chava, K. M. Daniels, M. V. S. Chandrashekhar, and A. B. Greytak, "Sub-bandgap response of graphene/sic schottky emitter bipolar phototransistor examined by scanning photocurrent microscopy," 2D Mater. 5, 011003 (2017).
- ⁴B. Ecker, J. C. Nolasco, J. Pallarés, L. F. Marsal, J. Posdorfer, J. Parisi, and E. von Hauff, "Degradation effects related to the hole transport layer in organic solar cells," Adv. Funct. Mater. 21, 2705 (2011).
- ⁵Z. Zolfaghari, E. Hassanabadi, D. Pitarch-Tena, S. J. Yoon, Z. Shariatinia, J. van de Lagemaat, J. M. Luther, and I. Mora-Seró, "Operation mechanism of perovskite quantum dot solar cells probed by impedance spectroscopy," ACS Energy Lett. 4, 251 (2019).
- ⁶A. K. Rath, T. Lasanta, M. Bernechea, S. L. Diedenhofen, and G. Konstantatos, "Determination of carrier lifetime and mobility in colloidal quantum dot films via impedance spectroscopy," Appl. Phys. Lett. 104, 063504 (2014).
- ⁷M. M. Tavakoli, A. Simchi, R. Tavakoli, and Z. Fan, "Organic halides and nanocone plastic structures enhance the energy conversion efficiency and self-cleaning ability of colloidal quantum dot photovoltaic devices," J. Phys. Chem. C 121, 9757 (2017).
- ⁸T. Fukuda, A. Takahashi, H. Wang, K. Takahira, T. Kubo, and H. Segawa, "Impedance analysis of PbS colloidal quantum dot solar cells with different ZnO nanowire lengths," Jpn. J. Appl. Phys., Part 1 57, 03EJ02 (2018).
- ⁹N. Tessler, "Experimental techniques and the underlying device physics," J. Polym. Sci., Part B: Polym. Phys. **52**, 1119 (2014).
- ¹⁰D. Bozyigit and V. Wood, "Electrical characterization of nanocrystal solids," J. Mater. Chem. C 2, 3172 (2014).
- ¹¹G. Konstantatos, J. Clifford, L. Levina, and E. H. Sargent, "Sensitive solution-processed visible-wavelength photodetectors" Nat. Photonics 1, 531 (2007)
- processed visible-wavelength photodetectors," Nat. Photonics 1, 531 (2007). ¹²S. Krause, H. Talabani, M. Xu, W. Moritz, and J. Griffiths, "Scanning photo-induced impedance microscopy—An impedance based imaging technique," Electrochim. Acta 47, 2143 (2002).
- ¹³Y. Gao, A. J. Wise, A. K. Thomas, and J. K. Grey, "Spectroscopic and intensity modulated photocurrent imaging of polymer/fullerene solar cells," ACS Appl. Mater. Interfaces, 8, 285 (2016).
- ¹⁴D. Bozyigit, S. Volk, O. Yarema, and V. Wood, "Quantification of deep traps in nanocrystal solids, their electronic properties, and their influence on device behavior," Nano Lett. 13, 5284 (2013).
- ¹⁵D. Bozyigit, M. Jakob, O. Yarema, and V. Wood, "Deep level transient spectroscopy (DLTS) on colloidal-synthesized nanocrystal solids," ACS Appl. Mater. Interfaces 5, 2915 (2013).
- ¹⁶F. Ulaby, M. Maharbiz, and C. Furse, Circuit Analysis and Design (Michigan Publishing, 2018).
- 17 E. von Hauff, "Impedance spectroscopy for emerging photovoltaics," J. Phys. Chem. C 123, 11329 (2019).
- ¹⁸G. Konstantatos, M. Badioli, L. Gaudreau, J. Osmond, M. Bernechea, F. P. G. de Arquer, F. Gatti, and F. H. L. Koppens, "Hybrid graphene-quantum dot phototransistors with ultrahigh gain," Nat. Nanotechnol. 7, 363 (2012).

- ¹⁹I. Nikitskiy, S. Goossens, D. Kufer, T. Lasanta, G. Navickaite, F. H. L. Koppens, and G. Konstantatos, "Integrating an electrically active colloidal quantum dot photodiode with a graphene phototransistor," Nat. Commun. 7, 11954 (2016).
 ²⁰M. O. Guerrero-Pérez and G. S. Patience, "Experimental methods in chemical
- ²⁶M. O. Guerrero-Pérez and G. S. Patience, "Experimental methods in chemical engineering: Fourier transform infrared spectroscopy—FTIR," Can. J. Chem. Eng. 98, 25 (2020).
- ²¹S. Dzsaber, M. Negyedi, B. Bernáth, B. Gyüre, T. Fehér, C. Kramberger, T. Pichler, and F. Simon, "A Fourier transform Raman spectrometer with visible laser excitation," J. Raman Spectrosc. 46, 327 (2015).
- ²²J.-S. Yoo and S.-M. Park, "An electrochemical impedance measurement technique employing fourier transform," Anal. Chem. 72, 2035 (2000).
- 23 M. L. Kelley, J. Letton, G. Simin, F. Ahmed, C. A. Love-Baker, A. B. Greytak, and M. V. S. Chandrashekhar, "Photovoltaic and photoconductive action due to PbS quantum dots on graphene/SiC Schottky diodes from NIR to UV," ACS Appl. Electron. Mater. 2, 134 (2020).
- ²⁴J. Yang, L. Guo, Y. Guo, W. Hu, and Z. Zhang, "Epitaxial graphene/SiC Schottky ultraviolet photodiode with orders of magnitude adjustability in responsivity and response speed," Appl. Phys. Lett. 112, 103501 (2018).
- ²⁵V. S. N. Chava, B. G. Barker, A. Balachandran, A. Khan, G. Simin, A. B. Greytak, and M. V. S. Chandrashekhar, "High detectivity visible-blind SiF4 grown epitaxial graphene/SiC Schottky contact bipolar phototransistor," Appl. Phys. Lett. 111, 243504 (2017).
- ²⁶T. Rauch, M. Böberl, S. F. Tedde, J. Fürst, M. V. Kovalenko, G. Hesser, U. Lemmer, W. Heiss, and O. Hayden, "Near-infrared imaging with quantum-dot-sensitized organic photodiodes," Nat. Photonics 3, 332 (2009).
- ²⁷J. Zhang, R. W. Crisp, J. Gao, D. M. Kroupa, M. C. Beard, and J. M. Luther, "Synthetic conditions for high-accuracy size control of PbS quantum dots," J. Phys. Chem. Lett. 6, 1830 (2015).
- ²⁸Y. Shen, M. Y. Gee, R. Tan, P. J. Pellechia, and A. B. Greytak, "Purification of quantum dots by gel permeation chromatography and the effect of excess ligands on shell growth and ligand exchange," Chem. Mater. 25, 2838 (2013).
- ²⁹ A. Roberge, J. H. Dunlap, F. Ahmed, and A. B. Greytak, "Size-dependent PbS quantum dot surface chemistry investigated via gel permeation chromatography," Chem. Mater. 32, 6588 (2020).
- ³⁰R. Graham and D. Yu, "SPCM in semiconductor nanostructures," Mod. Phys. Lett. B 27, 1330018 (2013).
- ³¹M. Shatalov, G. Simin, V. Adivarahan, A. Chitnis, S. Wu, R. Pachipulusu, V. Mandavilli, K. Simin, J. P. Zhang, J. W. Yang, and M. A. Khan, "Lateral current crowding in deep UV light emitting diodes over sapphire substrates," Jpn. J. Appl. Phys., Part 1 41, 5083 (2002).
- ³²M. Steer, Microwave and RF Design: A Systems Approach, 1st ed. (SciTech Publishing, Inc., Raleigh, NC, 2010).
- ³³A. R. Kirmani, G. Walters, T. Kim, E. H. Sargent, and A. Amassian, "Optimizing solid-state ligand exchange for colloidal quantum dot optoelectronics: How much is enough?," ACS Appl. Energy Mater. 3, 5385 (2020).
- ³⁴H. H. Kausch, D. G. Fesko, and N. W. Tschoegl, "The random packing of circles in a plane," J. Colloid Interface Sci. 37, 603 (1971).
- 35A. Balachandran, "High quality low offcut 4h-Sic epitaxy and integrated growth of epitaxial graphene for hybrid graphene/SiC devices," Doctoral dissertation (University of South Carolina, 2017).
- 36S. Wood, D. O'Connor, C. W. Jones, J. D. Claverley, J. C. Blakesley, C. Giusca, and F. A. Castro, "Transient photocurrent and photovoltage mapping for characterisation of defects in organic photovoltaics," Sol. Energy Mater. Sol. Cells 161, 89 (2017).
- 37H. T. Nguyen, S. Y. Ryu, A. T. Duong, and S. Lee, "Effects of 1,2-ethanedithiol concentration on performance improvement of quantum-dot LEDs," RSC Adv. 9, 38464 (2019).
- ³⁸C. R. Kagan and C. B. Murray, "Charge transport in strongly coupled quantum dot solids," Nat. Nanotechnol. 10, 1013 (2015).
- ³⁹S. Masala, V. Adinolfi, J.-P. Sun, S. D. Gobbo, O. Voznyy, I. J. Kramer, I. G. Hill, and E. H. Sargent, "The silicon:colloidal quantum dot heterojunction," Adv. Mater. 27, 7445 (2015).
- ⁴⁰V. Adinolfi and E. H. Sargent, "Photovoltage field-effect transistors," Nature 542, 324 (2017).
- ⁴¹S. U. Omar, T. S. Sudarshan, T. A. Rana, H. Song, and M. V. S. Chandrashekhar, "Interface trap-induced nonideality in as-deposited Ni/4H-SiC Schottky barrier diode," IEEE Trans. Electron Devices 62, 615 (2015).

- ⁴²T. Kim, M. L. Kelley, D. Kim, A. B. Greytak, and S. Jeong, "Purification of colloidal nanocrystals along the road to highly efficient photovoltaic devices," Int. J. Precis. Eng. Manuf.-Green Technol. (published online, 2020).
- J. Precis. Eng. Manuf.-Green Technol. (published online, 2020).

 43 J. Yang, D. Hahm, K. Kim, S. Rhee, M. Lee, S. Kim, J. H. Chang, H. W. Park, J. Lim, M. Lee, H. Kim, J. Bang, H. Ahn, J. H. Cho, J. Kwak, B. Kim, C. Lee, W. K. Bae, and M. S. Kang, "High-resolution patterning of colloidal quantum dots via non-destructive, light-driven ligand crosslinking," Nat. Commun. 11, 2874 (2020).
- C. D. Dieleman, W. Ding, L. Wu, N. Thakur, I. Bespalov, B. Daiber, Y. Ekinci,
 S. Castellanos, and B. Ehrler, "Universal direct patterning of colloidal quantum
- dots by (extreme) ultraviolet and electron beam lithography," Nanoscale 12, 11306 (2020).
- 45W. Zhou, L. Zheng, X. Cheng, W. Zhou, X. Xiao, K. Xu, W. Xin, P. Ye, and Y. Yu, "PbS colloidal quantum dots patterning technique with low vertical leakage current for the photodetection applications," J. Mater. Sci.: Mater. Electron. 31, 5900 (2020).
- 46R. Sliz, M. Lejay, J. Z. Fan, M.-J. Choi, S. Kinge, S. Hoogland, T. Fabritius, F. P. G. de Arguer, and E. H. Sargent, "Stable colloidal quantum dot inks enable inkjet-printed high-sensitivity infrared photodetectors," ACS Nano 13, 11988 (2019)